*Article*

# Characterization of Internal Defects and Fiber Distribution of BFRC Based on the Digital Image Processing Technology

Fengbin Chen [1], Bin Xu [1], Huazhe Jiao [1,*], Zhuen Ruan [2,*], Juanhong Liu [2], Xinming Chen [1], Liuhua Yang [1] and Zhen Li [1]

1   School of Civil Engineering, Henan Polytechnic University, Jiaozuo 454003, China; fbchen@hpu.edu.cn (F.C.); 211908020017@home.hpu.edu.cn (B.X.); 13782850808@163.com (X.C.); 212008020006@home.hpu.edu.cn (L.Y.); zhenli@hpu.edu.cn (Z.L.)
2   School of Civil and Resources Engineering, University of Science and Technology Beijing, Beijing 100083, China; juanhong1966@hotmail.com
*   Correspondence: jiaohuazhe@hpu.edu.cn (H.J.); ustb_ruanzhuen@ustb.edu.cn (Z.R.)

**Abstract:** Adding basalt fiber into concrete can significantly improve its mechanical properties. In order to explore the influence of basalt fiber content on the uniaxial compressive strength and splitting tensile strength of concrete and the mechanism of fiber action, this paper conducts compressive and splitting tensile tests on three kinds of basalt fiber concrete specimens with different fiber content and obtains the relationship between the macro mechanical properties and the fiber content. At the same time, with the help of CT scanning equipment and digital image processing technology, the microstructure of basalt fiber concrete with three groups of fiber content is reconstructed, and the pore, crack, and fiber distribution are quantitatively described using the calculation and processing function of the Avizo reconstruction software. The results show that when the optimal fiber content is 3 kg/m$^3$, the improvement rates of uniaxial compressive strength and splitting tensile strength are 31.9% and 23.7%, respectively. The network structure formed by fiber in concrete has the best compactness and the least number of pores, with an average sphericity of 0.89 and an average pore volume of 20.26 μm$^3$. Through analysis, it was found that the initial defects of basalt fiber concrete exist in the form of pores, and the addition of basalt fiber will destroy the large pore size of concrete, change the pore size distribution, and increase the average sphericity; The distribution of the fiber in the concrete is a three-dimensional network, and the distribution of the fiber in the initial defect distribution area is parallel to the direction of pore arrangement.

**Keywords:** basalt fiber reinforced concrete; fiber distribution; CT scanning; meso-structure

## 1. Introduction

Fiber has excellent mechanical properties and durability. In engineering practice, fiber is commonly used as a reinforcement material to improve mechanical properties, such as adding fiber into polymer composite material [1–3], concrete material, etc. [4–6]. Fiber reinforced concrete can improve concrete performance by effectively adding fiber into concrete. Compared to ordinary concrete, fiber reinforced concrete has excellent tensile strength, impact strength, elongation, crack resistance, ductility, and high temperature resistance [7–10]. Because of the different physical properties of various fibers, the effects of fiber on concrete are also very different. Basalt fiber, as a green environmental protection material, has high tensile strength, good alkali resistance, large elastic modulus and excellent interface shear strength, and low production cost. Therefore, using basalt fiber as a concrete reinforcement material is a good choice [11]. At present, the research on the mechanical properties of basalt fiber concrete is relatively mature [12,13]. It is agreed that basalt fiber can improve the tensile strength of concrete, but there are differences in the influence of basalt fiber on the compressive performance of concrete. Li et al. [14], through the BFRC mechanical properties experiment, found that when the fiber content

increases from 0.05% to 0.3%, the 7 d compressive strength and 28 d compressive strength decreased by varying degrees. According to the mechanical property test in reference [15], whether the fiber length was 6 mm or 12 mm, increasing the fiber causes the compressive strength to first increase and then decrease, while the flexural strength shows an increasing trend. Therefore, there is no consistent conclusion regarding the effect of basalt fiber on the compressive strength of concrete.

As a composite material, the macro properties of basalt fiber concrete are not only directly related to basalt fiber and the concrete matrix material, but also with meso-structure. The meso-structure has a great influence on the mechanical properties and damage mechanism of concrete. Therefore, mastering the variation law of the fine structure of basalt fiber concrete can create a more scientific explanation for problems that occur in the macro level of the concrete. The fine structure of basalt fiber concrete mainly includes fiber distribution, pore cracks, and other internal defects. At present, the research methods for fiber distribution are as follows: SEM scanning [16], mercury pressure, and the nuclear magnetic resonance method are used to analyze pore structure [17]. The research on fractures has been mainly conducted using the acoustic emission method and digital image correlation technology [18]. If we want to study the fine structure of basalt fiber concrete, two or more methods are usually needed to realize results, and these methods also have different limitations. For example, the microstructure area of concrete that can be observed by SEM is very small, and the results are often limited by the observation area [19,20]; the results of the mercury compression method are easily affected by the structure type and shape of the holes in concrete samples, which caused the the measurement results to be discrete and have large errors; the porosity measured by NMR is mainly concentrated on nano gel holes, and this type of pore has little effect on the concrete performance. When the crack is measured using the acoustic emission method, crack propagation information can only be obtained by changing characteristic parameters, and the quantitative description of the cracks is not available. Therefore, a comprehensive characterization method for basalt fiber reinforced concrete fine structure is needed.

In the 1980s, CT technology was applied to the research of concrete materials, and nondestructive concrete testing was realized. However, in the early development of this technology, only two-dimensional CT images could be obtained after CT scanning the concrete, and the relevant information was recorded and saved in the digital form on a computer. In recent years, with the improvement of computer processing ability, the use of a computer can realize the commands of CT image denoising, filtering, image segmentation, so as to build a three-dimensional model of concrete, which is called digital image processing technology [21–24]. At present, there is a variety of research on the processing of CT scanning images of fiber reinforced concrete with digital image processing technology, but there is little research on the microstructure of basalt fiber reinforced concrete with this technology [25]. For example, in reference [26], the concrete aggregate, pores, and other structures were extracted using digital image processing technology. In reference [27], the damage process of the concrete meso-structure under uniaxial compression was studied by CT technology. Based on traditional digital image processing technology, a convolution neural network method for the segmentation and extraction of concrete meso-structure cracks in a CT scanning image is proposed. The cracks and pores are segmented and reconstructed, and the effectiveness of the method is verified. Based on CT scanning images and Avizo software, Rios studied the pore structure of high-strength self-compacting concrete mixed with polypropylene fiber. On the basis of obtaining the three-dimensional reconstruction model of the specimen, it quantitatively expressed the pore number and pore size distribution and obtained the influence of polypropylene fiber on the micro pore structure of concrete [28]. Vicente et al. took steel fiber reinforced concrete as the object of study and first conducted CT scanning on it; imported the two-dimensional image obtained from the scanning into the reconstruction software, Avizo; established the fiber distribution model; and quantitatively characterized the steel fiber with spatial angle and efficiency index, showing the synergistic effect of fiber from the quantitative and

qualitative angles [29]. In reference [30], X-ray computed tomography and digital image processing techniques were used to reconstruct the pore and crack distribution maps of plain concrete and boron–basalt fibers concrete, and the pore diameter distribution and volume parameters were quantitatively characterized. The results showed that the basalt fiber implanted with boron oxide limited the microcrack area.

In this paper, based on three kinds of basalt fiber content, splitting tensile and compression experiments are conducted to explore the influence of basalt fiber content on the uniaxial strength and splitting tensile strength of concrete, and the best fiber content is obtained. At the same time, the microstructure of basalt fiber reinforced concrete is reconstructed using CT scanning and digital image processing technology. The microstructure characteristics of basalt fiber reinforced concrete are described qualitatively and quantitatively. The influence of basalt fiber on the microstructure of concrete and its mechanism are analyzed.

## 2. Materials and Methods

### 2.1. Materials

The base concrete was designed according to the strength grade C30, the cement was 42.5 ordinary silicate cement, the sand was made of machine-made sand, the coarse aggregate was made of crushed stone with the maximum particle size not exceeding 10 mm, the basalt fiber is 18 mm basalt fiber was produced by Shanxi Jintou Basalt Development Company, and the water was ordinary tap water. Based on the idea of the fiber volume rate method, the fibers were added directly to the specimens when they were made to the specifications of the design of the base concrete mix. The BFRC mixing is shown in Table 1. Each specimen group was dosed with basalt fiber as the variable, the dosage range was 0–6 kg/m$^3$, and the unit variable was 3 kg/m$^3$. The size of the specimen used in the uniaxial compression test was a cube with a diameter of 25 mm and a height of 50 mm. In the splitting tensile test, the specimen size was 100 mm cube. The specimens are shown in Figure 1.

**Table 1.** The mix proportion of plain concrete kg/m$^3$.

| Cement | Cobble | Sand | Water | Accelerator |
|--------|--------|------|-------|-------------|
| 440 | 880 | 880 | 260 | 17.6 |



**Figure 1.** The specimen.

### 2.2. Methods

#### 2.2.1. CT Scanning

The equipment used for CT scanning was the Phoenix V | tome | x s series X-ray CT scanner from GE, Germany, as seen Figure 2a, which is able to perform observations down to 0.5 μm, and the sample placement table is shown in Figure 2b.
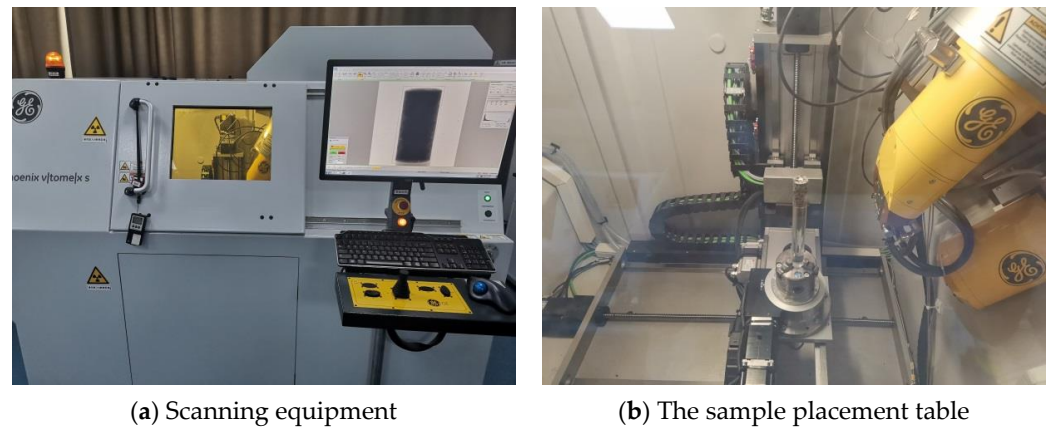
(**a**) Scanning equipment



(**b**) The sample placement table

**Figure 2.** CT scanning equipment.

When scanning the specimen, the probe of the industrial CT scanning equipment emits X-rays, and the intensity of the X-rays after penetrating the concrete will be different because of the different X-ray absorption ability of the internal concrete material. After converting these light signals into digital signals, the horizontal and vertical slice information maps are obtained. Figure 3 shows the horizontal slice map the fiber dosage of which is $3 \, \text{kg/m}^3$. Through the slice map, the distribution of pores, cracks, and aggregates can be visualized, but the slice map can only reflect the two-dimensional structural information of the internal material and cannot realize the quantitative characterization, which needs to be further processed using reconstruction software.
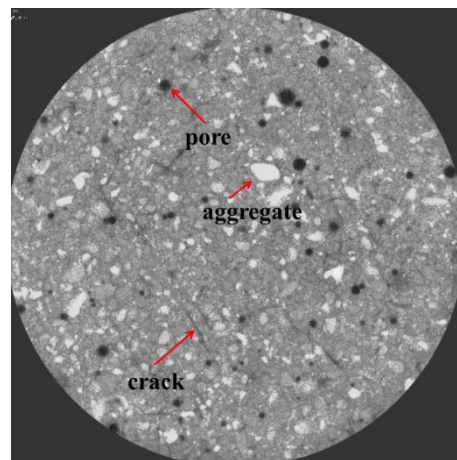


**Figure 3.** The horizontal slice.

2.2.2. Uniaxial Compression Experiment

Basalt fiber reinforced concrete with each fiber content consisting of three-cylinder specimens, were tested on a WES-1000b electro-hydraulic universal testing machine in accordance with IS Code Standard and the *Test Standard for Mechanical Properties of Ordinary Concrete* (GB/T50081-2002) [12,13,25]. In the test results, the arithmetic mean value of 3 specimens was used as the compressive strength value of the group of specimens. If the difference between the maximum value and the minimum value and the intermediate value was not more than 15% of the intermediate value, the intermediate value was taken as the compressive strength value of the group of specimens. If the difference between the two values and the median value was greater than 15% of the median value, the group of test results was invalid. The placement status of the specimen on the universal press is shown in the Figure 4.
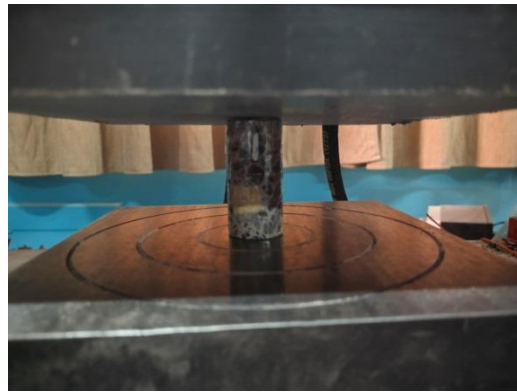
**Figure 4.** Loading diagram of specimen.

2.2.3. Tensile Strength Experiment

When the splitting tensile strength test was conducted for three groups of fiber rein-forced concrete, the basalt fiber concrete with fiber content of each group contained three 100 mm cube specimens, which were carried out according to the standard of IS-5816 and the *Test Standard for Mechanical Properties of Ordinary Concrete* (GB/T50081-2002) [12,31,32]. The test strip adopted an 80 mm diameter steel arc-shaped cushion strip, the length of the strip was not less than the side length of the test piece. The wooden backing plate was placed between the cushion strip and the sample, the width of the backing plate was 20 mm, the thickness of 3–4 mm was not less than the side length of the test piece, and the backing plate could not be reused. See the Figure 5 for the loading diagram and the actual diagram.
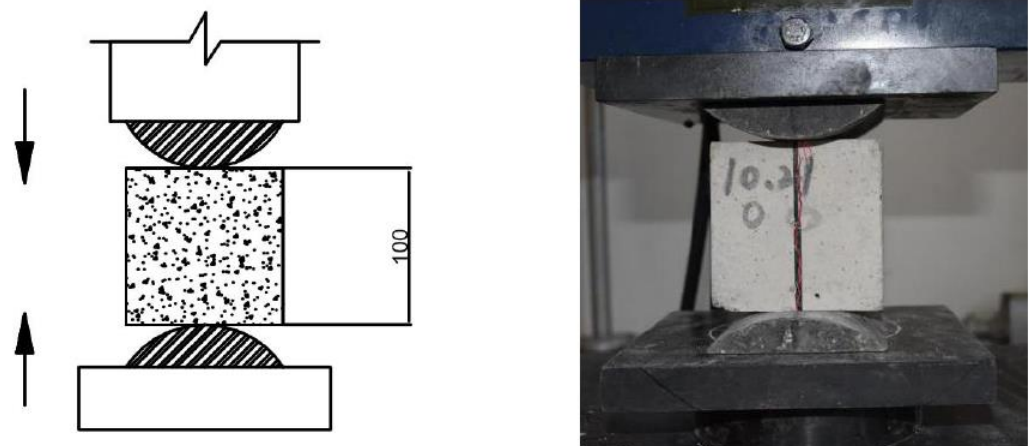


**Figure 5.** Loading diagram of specimen of tensile strength experiment.

## 3. Results

### 3.1. Mesostructure Reconstruction

The slice map obtained by the CT scanning equipment could only reflect two-dimensional information and could not realize the quantitative characterization of the spatial structure. In this paper, based on the reconstruction and calculation functions software Avizo, the 2D slice map was stacked and reconstructed to obtain a 3D reconstructed model of the microstructure. Considering computer operation processing capacity, a region of $200 \times 200 \times 200$ voxels was uniformly selected for reconstruction in this paper [33,34].

3.1.1. Internal Defect

There were a large number of internal defects such as pores and cracks in the concrete, and the distribution of pores and cracks could be directly observed based on the slices obtained from the CT scanning. However, the quantitative statistics and characterization

of these defective structures could not be achieved, which would cause the effect of the fiber dosage on the original defect in concrete to not be reflected.

The reconstruction software Avizo could effectively solve this problem by determining the appropriate threshold value through image processing. In this way, the distribution of pores and cracks inside the concrete could be reconstructed in the Avizo software. Figure 6 shows the distribution of internal defects structure in the area taken from a specimen with a different fiber dosage mainly including pores and cracks, which are rendered into different colors according to the volume and surface area size. It is easy to see that there are more pores and cracks inside the plain concrete, mostly distributed in the approximate horizontal direction. The volume is larger, and in the middle part, a red line of fissures can be clearly observed in an inclined direction, with a longer length, while the number of long cracks is significantly reduced in the specimens mixed with basalt fibers, and the pores and cracks are mostly present in a small volume.
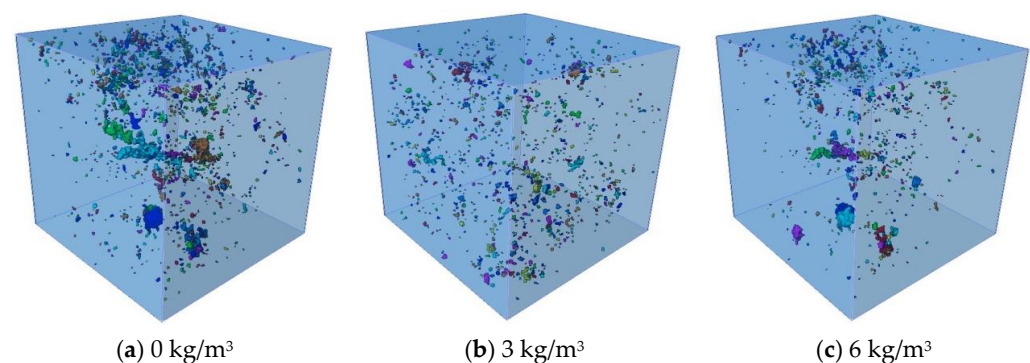


(**a**) 0 kg/m³        (**b**) 3 kg/m³        (**c**) 6 kg/m³

**Figure 6.** The distribution of pore and crack of specimens.

(1)   Sphericity analysis

The internal concrete defects mostly exist in the form of pores and cracks. Through consulting references [35], it can be found that the cracks and pores can be distinguished according to the size of the sphericity. According to the Formula (1), the maximum sphericity is 1, and the corresponding shape is a sphere. The sphericity of other shapes is less than 1. The closer shape is to a sphere, the greater the sphericity. For example, the sphericity of a 20hedron can reach 0.939, but the sphericity of the tetrahedron is 0.671. Combined with this knowledge of geometry, the surface area of the sphere is the smallest when the volume is the same. For concrete, the smaller the pore surface area is, the higher the density and strength of concrete will be.

$$\varphi = \frac{\sqrt[3]{\pi(6V)^2}}{A} \tag{1}$$

Through the statistics of sphericity in Figure 7, it can be found that the sphericity of the three groups of specimens is not less than 0.3, which indicates that the corresponding internal defects of the three kinds of specimens mainly exist in the form of pores. It can be seen from the figure below that the distribution of the pore sphericity of the concrete will change after adding basalt fiber. When the fiber content is 3 kg/m³, compared to ordinary concrete, the proportion of pores with sphericity less than 0.6 decreases significantly, making the proportion of pores corresponding to larger sphericity increase, indicating that basalt fiber can destroy the internal pore morphology of concrete; When the fiber content is 6 kg/m³, the proportion of pores with sphericity between 0.6 and 0.8 decreases. In addition to the increase of the proportion of pores between 0.8 and 1.0, the proportion of pores with sphericity between 0.4 and 0.6 also increases. It may be that the fiber content increases, which destroys the original pores and makes the pores develop into an irregular shape due to the amount of fiber. It can be seen that the average sphericity of ordinary concrete is

0.876. With the increase of fiber content, the average sphericity gradually increases, but the average sphericity changes little with the change of fiber content. When the fiber content is 3 kg/m$^3$ and 6 kg/m$^3$, the corresponding average coordination number is 0.89 and 0.902, respectively, which indicates that the original pore morphology will be destroyed after the addition of fiber content, making the pores more regular as a whole. However, this effect is less affected by the change of fiber content.
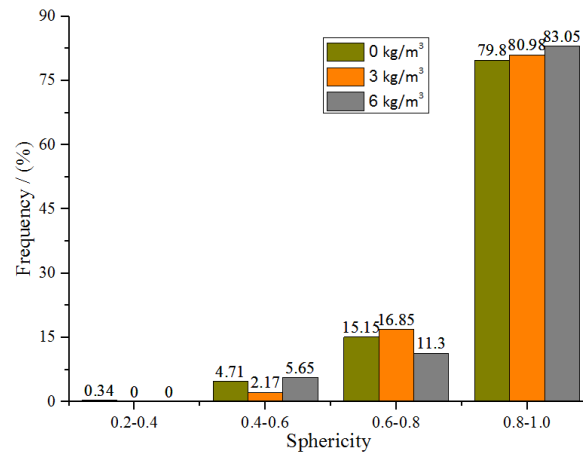


**Figure 7.** Distribution of sphericity.

(2) Quantitative statistics

Table 2 lists the number of pores, the average volume, and the average surface area in the ROI reconstruction area of the three specimens. Overall, the fiber dosage has a large effect on the number of pores, and the number of pores is the least at the fiber dosage of 3 kg/m$^3$. The number of pores increases slightly at the fiber dosage of 6 kg/m$^3$, but still shows a decreasing trend compared with plain concrete, indicating that the addition of fiber will destroy the production of original pores in concrete, which is reflected by the number of pores decreasing and then increasing. In addition, the fiber will also affect the volume and surface area of the pores, which will lead to a decrease in the average surface area and average volume of the pores. This is probably because the fiber dosage causes a portion of the pore to be penetrated. The cement mortar enters, and the pore is filled. The effect is related to the fiber dosage. The greater the dosage, the more obvious the effect is. When the fiber dosage is large, the fiber will appear as agglomeration in some areas, and new pores will be formed between the fibers.

**Table 2.** Statistics of pore structure of BFRC specimens with different fiber dosages.

| Fiber Dosage/kg m$^{-3}$ | Average Surface Area/μm$^2$ | Average Volume/μm$^3$ | Number |
|---|---|---|---|
| 0 | 33.31 | 24.82 | 1356 |
| 3 | 28.58 | 20.26 | 841 |
| 6 | 19.70 | 10.63 | 1073 |

This result is contrary to the research results of Zhang et al. [36] found that basalt fiber would pass through the pores and fissures using SEM. When the fiber content increased, the number of micropores increased. On the other hand, Zhang et al. [37] measured the pore size of basalt fiber concrete using the mercury intrusion method and found that basalt fiber can reduce the number of harmful pores and multi harmful pores in concrete. However, the influence of the fibers obtained in this paper on the pore size of concrete is only reflected in the average surface area and average volume. Although the visualization of microstructures such as pores is realized, there are still some deficiencies in the quantitative statistics.

### 3.1.2. Fiber Distribution

Assuming that the basalt fibers distributed within the concrete are not bent, based on the search cone algorithm, the fibers will be divided into a number of small sections and the coordinates of the start and end points of that fiber can be obtained, respectively. In this way, a model of fiber distribution can be obtained.

The model of fiber distribution in Figure 8 shows the fiber distribution at the fiber dosage of 3 kg/m$^3$ and 6 kg/m$^3$. In order to fully compare the three groups of specimens, the reconstructed part of the plain concrete is shown in grey, as in Figure 8a. Most of the fibers inside the concrete are distributed in an approximately horizontal state regardless of the fiber dosage, and the number of vertically distributed fibers is low. This feature is most evident at the fiber dosage of 6 kg/m$^3$. In Figure 8b, the fibers are distributed in all directions, except for a few local areas where the distance between fibers is moderate and there is no obvious fiber agglomeration. In Figure 8c, the number of fibers increases, the fiber spacing decreases, and the proportion of fibers distributed horizontally increases significantly. Additionally, the phenomenon of fiber accumulation occurs in dense areas, while some areas are missing this phenomenon due to missing fibers.
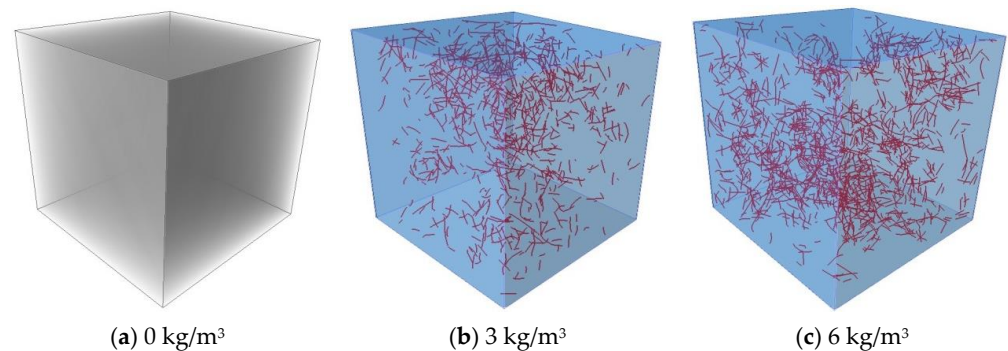


(**a**) 0 kg/m³      (**b**) 3 kg/m³      (**c**) 6 kg/m³

**Figure 8.** The model of fiber distribution.

In Avizo, the fiber distribution model can be obtained based on the search cone algorithm, which treats fibers as cylinders and achieves quantitative fiber statistics by counting the two distribution angles in the spatial coordinate system.

In Figure 9, θ is the polar angle, which represents the angle between the fiber and Z-axis ranging from 0–90°. And φ is the azimuth angle, which represents the angle between the projection of the fiber on the horizontal plane and the positive axis of *X*-axis ranging from 0–360°.
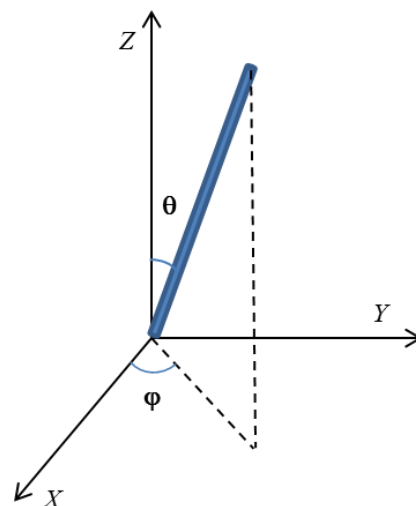


**Figure 9.** The fiber orientation.

The distribution of φ is more uniform, indicating that the fibers will interlock and overlap in the internal space of the concrete, so the fibers can form a dense mesh structure together. The value θ reflects the inclination degree of the fibers, and the larger the angle, the more inclined the fibers are, and the more they tend to be distributed in a horizontal direction.

The fiber spatial distribution angles are represented in polar coordinates in the form of polar angles and polar diameters using the statistics of the two angles θ and φ in the model of fiber distribution, as shown in Figure 10. In Figure 10, the polar diameter is represented as θ and the polar angle as φ. By observing the density of the distribution of the points in the concentric circles, the uniformity of the distribution of the fibers on the horizontal plane can be obtained. The more uniform the distribution of the points in the concentric circles, the better the denseness of the mesh structure formed by the fibers. By observing the dispersion of the points inside the sector, the vertical distribution of the fibers can be obtained. The corresponding larger pole diameter indicates that the distribution state of fiber tends to be of a more horizontal distribution. From the distribution of points in Figure 10a,b, the fibers under both doping levels can form a dense mesh structure inside the concrete, and most of the fibers in the two groups of specimens correspond to θ greater than 45°, indicating that most of the fibers inside the concrete are distributed in an approximately horizontal direction. Second, the distribution of all points in the two figures within each concentric circle area is not obviously missing, indicating that the basalt fibers are distributed in all areas inside the concrete. When the fiber dosage changed from $3 \, \text{kg/m}^3$ to $6 \, \text{kg/m}^3$, the distribution of points in Figure 10b appeared concentrated in some areas, which may cause the phenomenon of fiber agglomeration and crossover inside the concrete due to the increase of fiber dosage.
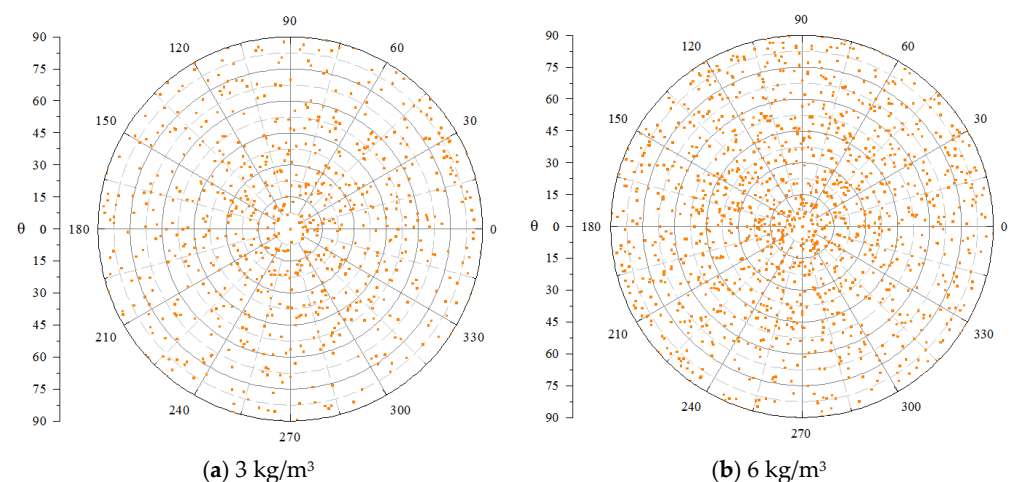


(**a**) 3 kg/m³　　　　　　　　　　　　　　　　　(**b**) 6 kg/m³

**Figure 10.** The distribution of fiber angle.

### 3.2. The Uniaxial Compressive Strength

The uniaxial compression experiments were conducted on three groups of cylindrical specimens, and the damage morphology of the specimens is shown in Figure 11. By comparing the morphology of the three groups of specimens after being damaged, it can be seen that the crack distribution of the cylindrical specimens after being damaged is related to the level of fiber dosage. For the plain concrete, the surface peeling phenomenon is obvious when the specimens are damaged, and there are more cracks. At the same time, the crack distribution is usually concentrated on the interior of the peeling part, as shown in Figure 11a. However, the specimens mixed with basalt fibers are damaged and there are less cracks. The peeling phenomenon is not obvious. This performance is related to the level of fiber dosage, and the best effect is achieved at the fiber dosage of $3 \, \text{kg/m}^3$, where only short cracks appear on the surface of the specimens after destruction, as shown in Figure 11b,c [18].

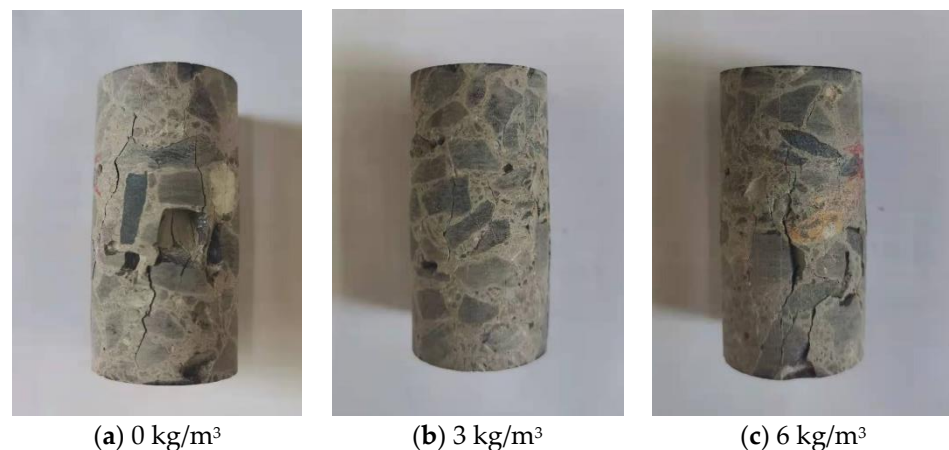| (**a**) 0 kg/m³ | (**b**) 3 kg/m³ | (**c**) 6 kg/m³ |

**Figure 11.** Experimental failure mode of compressive strength of test blocks with different fiber content.

The uniaxial compression experiments reveal that the strength of plain concrete could reach 32.736 MPa, and the strength would increase with the addition of basalt fibers, and the increase is related to the fiber dosage amount. The highest strength of 43.168 MPa (31.9% increase) was achieved at 3 kg/m³ and the lower strength of 35.648 MPa (8.9% increase) was achieved at 6 kg/m³.

### 3.3. The Tensile Strength

During the experiment, it was found that the cracks tend to appear near the middle line of the upper surface of plain concrete and split into two parts along a straight crack after being destroyed, showing brittle failure, and there are many bending cracks in the splitting failure of concrete mixed with basalt fiber. The main reason for this is that the basalt fiber disperses the tensile stress trend inside the concrete, reduces the intensity of crack cracking, and causes the cracks to distribute themselves in a curved direction. Through the comparison of three groups of 28 d splitting tensile strength in Figure 12, it was found that two kinds of fiber content can improve the splitting tensile performance of concrete, and the improvement effect of tensile strength is related to the fiber content. When the fiber content is 3 kg/m³, the improvement rate is the largest and can reach 23.7%. When the fiber content increases to 6 kg/m³, the tensile performance of the basalt fiber concrete decreases, but it is still higher than that of plain concrete. The research results are similar to those of B. Ramesh et al. B. Ramesh et al. carried out the splitting tensile strength experiment of basalt fiber reinforced concrete cylinder blocks with different fiber content (0–2.0%) and found that the four groups of fiber content all enhanced the splitting tensile strength and that the best content was 1.5% [12].
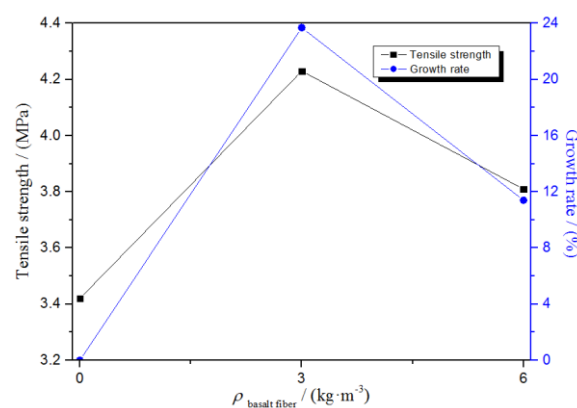


**Figure 12.** Tensile strength and its increasing range.

### 3.4. The Function Mechanism of Fiber

Taking the reconstructed area in the 3 kg/m$^3$ specimen as an example, the distribution of pores and cracks and basalt fibers is reconstructed, as shown in Figure 9. It is clear from the Figure 13 that in the areas where the distribution of pores and cracks is more concentrated, the fiber spacing is smaller, and some of the fibers will cross the pores and cracks. When the concrete is subjected to the expansion of the cracks, the excellent tensile properties of the basalt fibers can be brought fully into play, and the fibers can effectively prevent the further development and expansion of the pores and cracks under this effect.
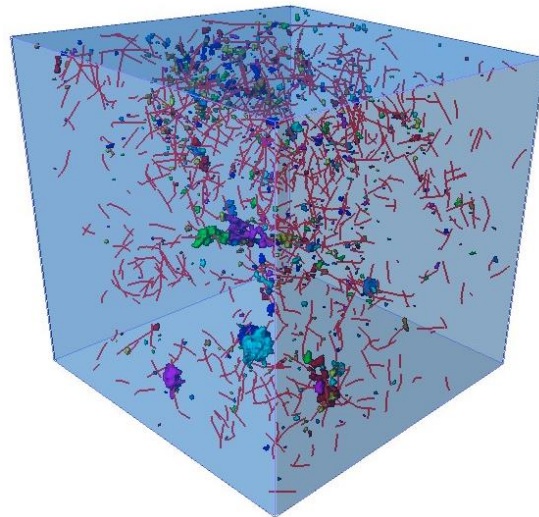


**Figure 13.** The distribution of crack and basalt fiber.

In addition, as a whole, the fibers form a spatially distinct mesh structure around the cracks, especially in the upper part of Figure 13, where a large number of pores and cracks are distributed, and the corresponding fibers are distributed more densely, with the fibers interlocking with each other. Therefore, when the concrete is subjected to load and a crack is developed, the fibers running through the crack can prevent the further development of that crack. Additionally, the mesh structure formed by the other fibers can prevent the concrete from shedding the internal aggregates and other materials, ensuring the structural integrity of the concrete after the expansion of the pores and cracks.

In combination with the uniaxial compression strength of the cylindrical concrete specimens, the uniaxial compression strength is greatest at the fiber dosage of 3 kg/m$^3$. According to the statistics of the number of initial pores and cracks and related parameters in Table 2, the initial imperfections inside the concrete are significantly improved, the distribution of basalt fibers is also more uniform, and the spatial mesh structure form around the pores and crack is better. As such, the uniaxial compressive strength is effectively improved. When the fiber dosage is 6 kg/m$^3$, the number of pores and cracks are only slightly reduced compared to plain concrete, and the initial imperfections inside are still high. Furthermore, due to the increase in the number of fibers and the decrease in the fiber spacing, the basalt fibers are missing in space, which affects the effect of the spatial mesh structure and creates the increase in uniaxial compressive strength.

### 4. Conclusions

(1)    When the fiber content is 3 and 6 kg/m$^3$, basalt fiber can enhance the uniaxial compressive strength and the splitting tensile strength of the concrete. The reinforcement degree is related to the fiber content. The best fiber content is 3 kg/m$^3$, and the increase rate of uniaxial compressive strength and splitting tensile strength is 23.7% and 31.9%, respectively;

(2) Based on the BFRC two dimensional CT slices of three fiber content groups, the fine structure reconstruction is realized by combining digital image processing technology. It was found that the initial defects of the plain concrete and basalt the fiber concrete were all in the form of pores. After adding fiber into concrete, the fiber reduced the number of pores and destroyed the original pore size and present situation, which is by the average surface area and average volume of pores decreasing and the average spherical degree increasing;

(3) Basalt fiber is distributed in the concrete mesh. From the statistical fiber distribution angle, it was found that when the fiber content is $3 \, \mathrm{kg/m^3}$, the density of the network structure was stronger than when the fiber content was $6 \, \mathrm{kg/m^3}$. In the areas with dense pore distribution, the amount of fiber distribution was higher. When the adjacent pores go through the sample, the fiber network structure can effectively avoid the concrete from breaking.

**Institutional Review Board Statement:** Not applicable.

**Informed Consent Statement:** Not applicable.

**Data Availability Statement:** Not applicable.

**Conflicts of Interest:** The authors declare no conflict of interest.

# References

1. Kushvaha, V.; Tippur, H. Effect of filler shape, volume fraction and loading rate on dynamic fracture behavior of glass-filled epoxy. *Compos. Part B Eng.* **2014**, *64*, 126–137. [CrossRef]
2. Sharma, A.; Kumar, S.A.; Kushvaha, V. Effect of aspect ratio on dynamic fracture toughness of particulate polymer composite using artificial neural network. *Eng. Fract. Mech.* **2020**, *228*, 106907. [CrossRef]
3. Kushvaha, V.; Kumar, S.A.; Madhushri, P.; Sharma, A. Artificial neural network technique to predict dynamic fracture of particulate composite. *J. Compos. Mater.* **2020**, *54*, 3099–3108. [CrossRef]
4. Fiore, V.; Scalici, T.; Di Bella, G.; Valenza, A. A review on basalt fibre and its composites. *Compos. Part B Eng.* **2015**, *74*, 74–94. [CrossRef]
5. Zhu, J.-P.; Chen, Y.; Zhang, L.; Guo, B.-K.; Fan, G.-X.; Guam, X.-M.; Zhao, R.-Q. Revealing the doping mechanism of barium in sulfoaluminate cement clinker phases. *J. Clean. Prod.* **2021**, *295*, 126405. [CrossRef]
6. Jiang, L.-C.; Yang, C.; Jiao, H.-Z. Ultimately exposed roof area prediction of bauxite deposit goaf based on macro joint damage. *Int. J. Min. Sci. Technol.* **2020**, *30*, 699–704. [CrossRef]
7. Hassani Niaki, M.; Fereidoon, A.; Ghorbanzadeh Ahangari, M. Experimental study on the mechanical and thermal properties of basalt fiber and nanoclay reinforced polymer concrete. *Compos. Struct.* **2018**, *191*, 231–238. [CrossRef]
8. Hedjazi, S.; Castillo, D. Relationships among compressive strength and UPV of concrete reinforced with different types of fibers. *Heliyon* **2020**, *6*, e03646. [CrossRef]
9. Jackiewicz-Rek, W.; Drzymała, T.; Kuś, A.; Tomaszewski, M. Durability of High Performance Concrete (HPC) Subject to Fire Temperature Impact. *Arch. Civ. Eng.* **2016**, *62*, 73–94. [CrossRef]
10. Jiang, L.-C.; Lai, X.-W.; Jiao, H.-Z. Concrete relative velocity prediction to prevent mortar segregation for safe gravity transporta-tion. *Alex. Eng. J.* **2020**, *59*, 5155–5164. [CrossRef]
11. Mohammadyan, Y.S.E.; Abbastabar, A.H.; Ahevani, O.N.; Shokravi, H.; Rahimian, K.S.S.; Petrů, M. Thermal performance of alginate concrete reinforced with basalt fiber. *Crystals* **2020**, *10*, 779. [CrossRef]
12. Ramesh, B.; Eswari, S. Mechanical behaviour of basalt fibre reinforced concrete: An experimental study. *Mater. Today Proc.* **2021**, *43*, 2317–2322. [CrossRef]
13. Meyyappan, P.L.; Jemimah, C.M. Studies on strength properties of basalt fibre reinforced concrete. *Mater. Today Proc.* **2021**. [CrossRef]

14. Li, M.; Gong, F.; Wu, Z. Study on mechanical properties of alkali-resistant basalt fiber reinforced concrete. *Constr. Build. Mater.* **2020**, *245*, 118424. [CrossRef]

15. Sun, X.-J.; Gao, Z.; Cao, P.; Zhou, C.-J. Mechanical properties tests and multiscale numerical simulations for basalt fiber reinforced concrete. *Constr. Build. Mater.* **2019**, *202*, 58–72. [CrossRef]

16. Wang, Y.; Hu, S.; He, Z. Mechanical and fracture properties of geopolymer concrete with basalt fiber using digital image correlation. *Theor. Appl. Fract. Mech.* **2021**, *112*, 102909. [CrossRef]

17. Xue, W.; Shen, L.; Jing, W.; Li, H. Permeability evolution and mechanism of thermally damaged basalt fiber-reinforced concrete under effective stress. *Constr. Build. Mater.* **2020**, *251*, 119077. [CrossRef]

18. Yang, L.-Y.; Xie, H.-Z.; Fang, S.-Z.; Huang, C.; Yang, A.-Y.; Chao, Y.-J. Experimental study on mechanical properties and damage mechanism of basalt fiber reinforced concrete under uniaxial compression. *Structures* **2021**, *31*, 330–340. [CrossRef]

19. Wang, D.-L.; Zhang, Q.-L.; Chen, Q.-S.; Qi, C.-C.; Feng, Y.; Xiao, C.-C. Temperature variation characteristics in flocculation settlement of tailings and its mechanism. *Int. J. Miner. Metall. Mater.* **2020**, *27*, 1438–1448. [CrossRef]

20. Zhang, Q.-L.; Li, Y.-T.; Chen, Q.-S.; Liu, Y.-K.; Feng, Y.; Wang, D.-L. Effect of temperatures and pH values on rheological properties of cemented paste backfill. *J. Cent. South Univ.* **2021**, *28*, 1707–1723.

21. Jiao, H.Z.; Wang, S.F.; Yang, Y.X.; Chen, X.M. Water recovery improvement by shearing of gravity-thickened tailings for cemented paste backfill. *J. Clean. Prod.* **2020**, *245*, 118882.

22. Jiao, H.-Z.; Wang, S.-F.; Wu, A.-X.; Shen, H.-M.; Wang, J.-D. Cementitious property of $NaAlO_2$-activated Ge slag as cement supplement. *Int. J. Miner. Met. Mater.* **2019**, *26*, 1594–1603. [CrossRef]

23. Chen, F.; Xu, B.; Jiao, H.; Chen, X.; Shi, Y.; Wang, J.; Li, Z. Triaxial mechanical properties and microstructure visualization of BFRC. *Constr. Build. Mater.* **2021**, *278*, 122275. [CrossRef]

24. Yang, Y.-X.; Zhao, T.-Q.; Jiao, H.-Z.; Wang, Y.-F.; Li, H.-Y. Potential effect of porosity evolution of cemented paste backfill on selective solidification of heavy metal ions. *Int. J. Environ. Res. Public Health* **2020**, *17*, 814. [CrossRef] [PubMed]

25. Zheng, D.; Song, W.-D.; Fu, J.-X.; Xue, G.-L.; Li, J.-J.; Cao, S. Research on mechanical characteristics, fractal dimension and internal structure of fiber reinforced concrete under uniaxial compression. *Constr. Build. Mater.* **2020**, *258*, 120351. [CrossRef]

26. Xing, C.; Xu, H.-N.; Tan, Y.-Q.; Liu, X.-Y.; Zhou, C.-H.; Scarpas, T. Gradation measurement of asphalt mixture by X-Ray CT images and digital image processing methods. *Measurement* **2019**, *132*, 377–386. [CrossRef]

27. Tian, W.; Cheng, X.; Liu, Q.; Yu, C.; Gao, F.-F.; Chi, Y.-Y. Meso-structure Segmentation of Concrete CT Image based on Mask and Regional Convolution Neural Network. *Mater. Des.* **2021**, *208*, 109919. [CrossRef]

28. Ríos, J.D.; Mínguez, J.; Martinez-De, L.C.A.; Vicente, M.Á.; Cifuentes, H. Microstructural analyses of the addition of PP fibres on the fracture properties of high-strength self-compacting concrete by X-ray computed tomography. *Constr. Build. Mater.* **2020**, *261*, 120499. [CrossRef]

29. Vicente, M.A.; Ruiz, G.; González, D.C.; Mínguez, J.; Tarifa, M.; Zhang, X. Effects of fiber orientation and content on the static and fatigue behavior of SFRC by using CT-Scan technology. *Int. J. Fatigue* **2019**, *128*, 105178. [CrossRef]

30. Skarżyński, Ł. Mechanical and radiation shielding properties of concrete reinforced with boron-basalt fibers using Digital Image Correlation and X-ray micro-computed tomography. *Constr. Build. Mater.* **2020**, *255*, 119252. [CrossRef]

31. American Society for Testing and Materials (ASTM). ASTM C39 Standard test method for compressive strength of cylindrical concrete specimens. In *Book of ASTM Standards*; American Society for Testing and Materials: Conshohocken, PA, USA, 2018.

32. Shi, F.; Pham, T.M.; Hao, H.; Hao, Y.-F. Post-cracking behaviour of basalt and macro polypropylene hybrid fibre reinforced concrete with different compressive strengths. *Constr. Build. Mater.* **2020**, *262*, 120108. [CrossRef]

33. Zhang, W.-Z.; Qiu, L. Characterization and analysis of pore structure of coal based on CT 3D reconstruction. *Coal Technol.* **2018**, *37*, 327–329.

34. Umbach, C.; Middendorf, B. 3D structural analysis of construction materials using high-resolution computed tomography. *Mater. Today Proc.* **2019**, *15*, 356–363. [CrossRef]

35. Liu, Z.-X.; Dong, S.-N.; Nan, S.-H.; Zhang, D.-Y.; Liu, D. Micro-CT analysis of void characteristics at the top of middle Ordovician limestone in Hanxing mining area. *J. Min. Saf. Eng.* **2021**, *38*, 343–352.

36. Zhang, L.-F.; Yin, Y.-L.; Yue, Y. Effect of basalt fiber content on mechanical performance of concrete. *Bull. Chin. Ceram. Soc.* **2016**, *35*, 2724–2728.

37. Zhang, L.-F.; Wang, D.-F. Effect of basalt fiber content on sulfate resistance and impermeability of concrete. *Bull. Chin. Ceram. Soc.* **2018**, *37*, 1946–1950.